

Article

Nitrogen-Doped Porous Carbon Nanosheets Based on a Schiff Base Reaction for High-Performance Lithium-Ion Batteries Anode

Mai Li, Zhi Cheng, Jingrui Sun, Yu Tian, Jiawei He, Yutian Chen, Yang Bai * and Zhiming Liu * 

Shandong Engineering Laboratory for Preparation and Application of High-Performance Carbon-Materials, College of Electromechanical Engineering, Qingdao University of Science and Technology, Qingdao 266061, China

* Correspondence: 03905@qust.edu.cn (Y.B.); zmliu@qust.edu.cn (Z.L.)

Abstract: Lithium-ion batteries (LIBs) have already gained significant attention because they have satisfactory energy density and no memory effect, making them one of the most widely used energy storage systems. In commercial LIBs, graphite is widely used as an anode material due to its excellent electrical conductivity and structural stability; however, as they are limited by their restricted theoretical capacity, there is an urgent need for the development of novel anode materials for LIBs. For this purpose, we designed a nitrogen-doped two-dimensional layered porous carbon material (2D-PNC) based on a covalent organic framework (COF) generated by a Schiff base reaction as a precursor. The characterization analysis results show that 2D-PNC is made of stacked two-dimensional ultra-thin carbon sheets with a porous structure. This unique structure is beneficial for electrolyte impregnation and lithium-ion storage, resulting in excellent electrochemical performance of 2D-PNC, which shows a high specific capacity of 573 mAh g⁻¹ after 380 cycles at 0.5 A g⁻¹. The results show that 2D-PNC provides the possibility of a practical application of high-performance lithium-ion batteries.

Keywords: Schiff base reaction; layered porous structure; covalent organic frameworks; lithium-ion batteries



Citation: Li, M.; Cheng, Z.; Sun, J.; Tian, Y.; He, J.; Chen, Y.; Bai, Y.; Liu, Z. Nitrogen-Doped Porous Carbon Nanosheets Based on a Schiff Base Reaction for High-Performance Lithium-Ion Batteries Anode. *Energies* **2023**, *16*, 1733. <https://doi.org/10.3390/en16041733>

Academic Editor: James M. Gardner

Received: 29 December 2022

Revised: 25 January 2023

Accepted: 6 February 2023

Published: 9 February 2023



Copyright: © 2023 by the authors. Licensee MDPI, Basel, Switzerland. This article is an open access article distributed under the terms and conditions of the Creative Commons Attribution (CC BY) license (<https://creativecommons.org/licenses/by/4.0/>).

1. Introduction

The growing demand for portable electronic equipment and electric automobiles in human society, coupled with the energy crisis and the growing interest in the renewable energy industry, has sparked extensive research into batteries by researchers. [1]. LIBs are attracting a lot of attention because of their satisfactory energy density, small self-discharge, and almost no memory effect [2–4]. The electrode material is one of the keys to lithium-ion battery performance [5]. Graphite is extensively used in commercial LIBs due to its structural stability and remarkable electrical conductivity [6]. However, because of its limited theoretical capacity (372 mAh g⁻¹), it cannot meet the growing demand for batteries [7].

Meanwhile, porous carbon materials are also among the ideal anode materials for lithium-ion batteries because of their porous structure and high specific surface area. These properties lead to better contact with the electrolytes to shorten the transport distance of Li⁺. In addition, porous carbon materials can obtain higher capacity and better rate performance than graphite, due to the expansion of the interlayer distance and the shortening of the ion transport pathways [8,9].

Moreover, heteroatoms (N, S, B, etc.) doping in the anode of carbon-based materials for lithium-ion batteries can also effectively enhance the electrochemical performance of lithium-ion batteries [10–13]. For example, the existence of nitrogen atoms improves the distance between carbon layers and generates huge amounts of defects, which then provides more active sites for the insertion of lithium ion [14]. Recently, significant developments have been achieved in the doping of initial carbon nanostructures with heteroatoms as

high-performance anode materials for LIBs [11,15], producing, for example, N-doped carbon nanoparticles [16], N-doped carbon nanofibers [12], and N, S-codoped porous graphene [10,17]. Although the combination of carbon materials and heteroatoms has excellent effects, developing novel hierarchical porous N-doped carbon materials with suitable morphology and appropriate levels of N-doping is still challenging.

Covalent organic frameworks (COFs) are a new category of organic porous carbon materials with excellent tunable two- or three-dimensional pore structures [18–20]. Their structures consist of covalent bonds formed between light elements (C, N, O, H, and B), and have the merits of uniform nanopore distribution and large specific surface area, which have shown promising applications in energy storage [21–23]. In this work, p-phenylenediamine and p-phthalaldehyde are used as raw materials to produce -C=N- linked COF as precursors through dehydration condensation through a Schiff base reaction. After that, the COF, melamine with and without zinc nitrate were carbonized to produce N-doped carbon (NC) or porous N-doped carbon (2D-PNC) for LIBs, wherein zinc nitrate was used as a pore-generating agent and melamine was used to further increase the nitrogen content of the material. 2D-PNC not only provides better electrolyte impregnation but also offers adequate sites for lithium-ion storage. With the merits of porous N-doped 2D nanostructure, 2D-PNC delivers a much more improved rate and cycling performance than NC. At the current density of 0.5 A g^{-1} , the discharge specific capacity reached 573 mAh g^{-1} after 380 cycles. The discharge specific capacity still reached 302 and 242 mAh g^{-1} at current densities of 3 A g^{-1} and 5 A g^{-1} .

2. Experiment

2.1. Preparation of COF, 2D-PNC, and NC

Zinc nitrate hexahydrate ($\text{Zn}(\text{NO}_3)_2 \cdot 6\text{H}_2\text{O}$), p-phenylenediamine (Pa), p-phthalaldehyde (Ppd), and melamine (MA) were purchased from Aladdin. Ethanol was purchased from Sinopharm. Acetate and acetonitrile were bought from Macklin. No further purification was performed on any of the reagents.

744 mg p-phthalaldehyde was mixed with 600 mg p-phenylenediamine in 100 mL ethanol and stirred for 15 min, then 5 mL acetate was added and stirred vigorously for 8 h. After the Schiff base reaction, the suspension was centrifuged with alcohol at 13,000 rpm for 8 min, washed three times, and dried overnight at $60 \text{ }^\circ\text{C}$ to finally acquire Pa-Ppd COF.

The as-prepared COF (0.6 g) was dissolved in acetonitrile (50 mL), and the MA (0.3 g) and $\text{Zn}(\text{NO}_3)_2 \cdot 6\text{H}_2\text{O}$ (1.2 g) were dissolved in 10 mL of deionized water (DIW). Subsequently, the solution containing MA and $\text{Zn}(\text{NO}_3)_2$ was poured into the acetonitrile solution containing COF. After stirring for 8 h, the above suspension was dried in an oven at $100 \text{ }^\circ\text{C}$ for 12 h. Following drying, the resulting solid was pyrolyzed in a tube furnace at $900 \text{ }^\circ\text{C}$ for 3 h under a floating inert gas atmosphere to finally obtain 2D-PNC. The synthesis method of NC was the same but without $\text{Zn}(\text{NO}_3)_2$.

2.2. Electrochemical Measurements

Electrochemical measurements of 2D-PNC and NC electrodes were conducted in a half-cell (coin cells, CR2025) test and assembled in an Ar-filled glovebox. The counter electrode was made of Li foil, the separator was Celgard 2400, and the nonaqueous electrolyte was 1 M LiPF₆ dissolved in a solution of ethylene carbonate and diethyl carbonate (1:1, v/v). To prepare the 2D-PNC working electrode, 80% of 2D-PNC active material, 10% of conductive carbon black (super P), and 10% of polyvinylidene fluoride (PVDF) were mixed with N-methyl-2-pyrrolidone (NMP). The obtained slurry was then homogeneously pasted onto the copper foil and dried under vacuum at $50 \text{ }^\circ\text{C}$ for 12 h. The loading of active mass on the electrode was about 1.2 mg cm^{-2} . The preparation method of the NC working electrode was the same as that of 2D-PNC except that the active material was replaced by NC. The LANHECT2001A battery test equipment was used to measure the LIBs' performance over the voltage range of 0.01–3.0 V. The cyclic voltammograms (CV, scan rates from 0.1 to 3.0 mV s^{-1}) curves were conducted with the CHI-760E electrochemical workstation

(Chenhua Instrument, Shanghai). A sine wave with an amplitude of 5.0 mV and a frequency range of 100 kHz to 0.01 Hz was used to acquire the EIS. The glovebox filled with Ar and H₂O with less than 0.1 ppm of oxygen and hydrogen was used to assemble all batteries.

2.3. Material Characterizations

Fourier transform infrared spectroscopy (FTIR) measurements were acquired from Thermo Scientific Nicolet iN10. SEM images were captured using a HITACHI SU8010 field emission scanning electron microscope. The XRD pattern was recorded on an X-ray diffractometer (Rigaku MiniFlex) with a scan range (2θ) of 3–90°, and the scanning rate was 3° per minute. Transmission electron microscopy (TEM) images and selected area electron diffraction (SAED) images were acquired on an FEI Talos 200S. X-ray photoelectron spectroscopy (XPS) spectra were used for Thermo Kalpha. BET analysis was obtained from Micromeritics ASAP2460. At room temperature, Raman spectroscopy was performed using a Renishaw InVia and an excitation wavelength of 532 nm. The BSD instrument system was used to evaluate Nitrogen (N₂) adsorption and desorption isotherms. A Brunauer-Emmett-Teller (BET) model was used for determining the surface area specific to each type of material.

3. Result and Discussion

The synthesis routes of Pa-Ppd COF and 2D-PNC are illustrated in Figure 1. Firstly, Pa and Ppd were dehydrated and condensed via a Schiff base reaction at room temperature, using the solution stirring method to form -C=N- linked COF. Subsequently, the as-prepared COF was mixed homogeneously with MA and Zn(NO₃)₂ in the solvent. Next, the above mixed suspension was dried and then the resulting solid was pyrolyzed to finally obtain 2D-PNC. The synthesis details are described in the experimental section. Zn(NO₃)₂ is gradually decomposed and volatilized during the pyrolysis process, resulting in the exfoliation of the carbon layer and porosity, which is also the key to the constitution of the two-dimensional porous layered structure of 2D-PNC. MA is introduced to enhance the N-doping level of 2D-PNC. In order to study the influence of the unique two-dimensional porous layered structure on the performance of LIBs, NC was also prepared. NC was prepared in the same way as 2D-PNC, except that Zn(NO₃)₂ was not added.

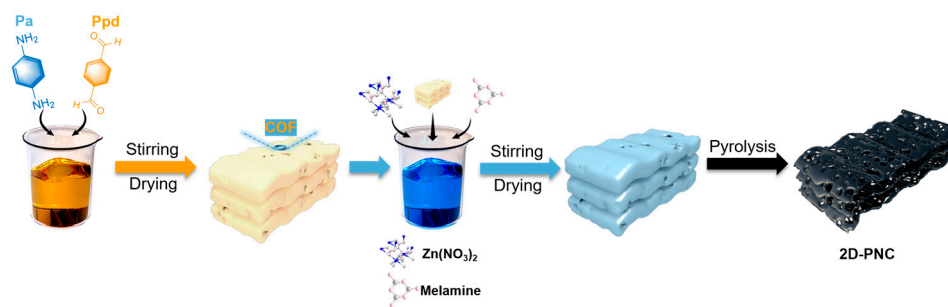


Figure 1. Schematic illustration of the synthesis of 2D-PNC.

In the Fourier transform infrared spectrum (FTIR), the disappearance of the peak at 1695 cm⁻¹ corresponds to the stretching vibration of the carbonyl groups, the disappearance of the peaks at 3303 and 3192 cm⁻¹ is ascribed to the -NH₂ stretching bands and the appearance of the peak at 1615 cm⁻¹ is ascribed to the stretching bands of C=N. The peak at 1220 cm⁻¹ can be ascribed to the C-N stretching bands (Figure 2a). This indicates that the COF is formed by dehydration condensation of Ppd with Pa by a Schiff base reaction under nonaqueous solvent. Subsequently, the synthesis of NC and 2D-PNC is carried out by the above synthesis method (Figure 1). Due to the loss of nitrogen-containing and carbon-containing groups in the pyrolysis process of COF, the chemical environment of 2D-PNC and NC is changed, resulting in a chemical shift of 30 cm⁻¹ at the characteristic peak of C=N. In addition, there is a peak at 1560 cm⁻¹ associated with the stretching

vibration of the C-N (Figure S1). Figure 2b shows the XRD pattern of NC and 2D-PNC. It can be seen that two distinct diffraction peaks appear at 23.5° and 42.8° for both materials, which correspond to graphite's (002) and (100) crystal planes [24]. No other impurity peaks are present that can explain the high purity of the NC and 2D-PNC. Meanwhile, the two diffraction peaks of 2D-PNC in the XRD pattern are weaker and broader compared to the NC, indicating a lower degree of graphitization of 2D-PNC [25]. A Raman spectroscopy test was performed to investigate the information of NC and 2D-PNC composition in depth, and Figure 2c shows the results. Both NC and 2D-PNC have two significant peaks around 1360 and 1590 cm^{-1} , which are two feature bands of the carbonaceous materials that correspond to the D-band (disorder carbon band) and the G-band (graphite carbon band), respectively [26]. The intensity ratios (I_D/I_G) of NC and 2D-PNC are 1.01 and 1.22, respectively, indicating a lower level of graphitization, a higher degree of disorder, and more defects in 2D-PNC, which agrees with the results in the XRD pattern. This results from the doping of N atoms in the 2D-PNC and the exposure of edges in the porous structure, which creates more defect sites [27]. These defect sites can offer more active sites in the following charging and discharging process, improving the lithium storage capacity of 2D-PNC [8].

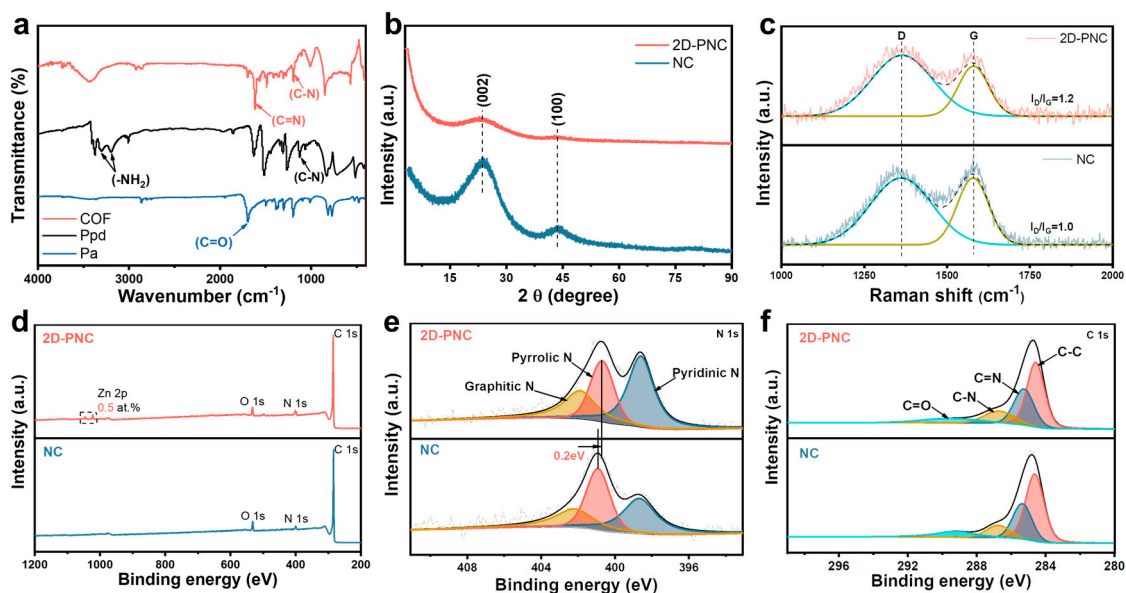


Figure 2. (a) FTIR of Pa-Ppd COF. (b) XRD pattern of 2D-PNC and NC. (c) Raman spectra of 2D-PNC and NC. (d) Typical XPS survey spectrum and corresponding (e) N 1s, (f) C 1s XPS spectra of the 2D-PNC and NC.

The XPS element survey of NC and 2D-PNC is presented in Figure 2d. NC is composed of C (1s, ~ 285 eV), O (1s, ~ 532 eV), and N (1s, ~ 401 eV). Additionally, 2D-PNC is mainly composed of C (1s, ~ 285 eV), O (1s, ~ 532 eV), and N (1s, ~ 401 eV), with a very low content (0.5 at.%) of Zn ($2p_{3/2}$, ~ 1022 eV). This is due to the low content of Zn remaining after the pyrolysis of $\text{Zn}(\text{NO}_3)_2 \cdot 6\text{H}_2\text{O}$ during the synthesis of 2D-PNC. $\text{Zn}(\text{NO}_3)_2 \cdot 6\text{H}_2\text{O}$ generates NO_x and H_2O gases during the pyrolysis process and forms ZnO nanoparticles. Then, ZnO is reduced by carbon to produce metallic Zn nanoparticles embedded in the carbon sheets, which evaporate at high temperatures. Porous structures and ultrathin carbon nanosheets are also believed to be formed by $\text{Zn}(\text{NO}_3)_2$ decomposition at high temperatures in 2D-PNC. The high-resolution XPS spectrum of Zn 2p from 2D-PNC is illustrated in Figure S2, which shows two peaks corresponding to the electronic states of $2p_{3/2}$ (1022 eV) and $2p_{1/2}$ (1045 eV) of Zn^0 , respectively. The $2p_{3/2}$ binding energy of Zn^{2+} (1021 eV) is lower than the standard of 1022 eV for Zn^0 , indicating that the remaining component in 2D-PNC should be Zn^0 rather than Zn^{2+} [28]. This is due to the vaporization residue of the Zn nanoparticles generated in the last step of the $\text{Zn}(\text{NO}_3)_2$ decomposition.

Due to its extremely low content, this also shows that the decomposition of $\text{Zn}(\text{NO}_3)_2$ is complete and thorough. The remaining Zn atoms can also improve the electrochemical performance of LIBs [29,30]. The high-resolution XPS spectrum of N 1s from 2D-PNC and NC (Figure 2e) can be classified into three types, including pyridinic N, pyrrolic N, and graphitic N. Compared with NC, the feature peak of pyrrolic N in 2D-PNC has a chemical shift of 0.2 eV, while the feature peaks of other N dopants are not changed in 2D-PNC. It appears that pyrrolic N was exposed to a different chemical environment in 2D-PNC than in NC, possibly due to the change in the chemical environment of pyrrole-type N caused by the Zn atoms remaining in 2D-PNC [28,31]. The high-resolution C 1s spectra of NC and 2D-PNC (Figure 2f) can be classified into four chemical components at 284.6, 285.3, 286.7, and 289.2 eV, corresponding to the C-C/C=C, C=N, C-N, and C=O bonds, respectively [32].

Figure 3a,b display the scanning electron microscopy (SEM) images of 2D-PNC, which reveal a distinct layered two-dimensional porous structure. In contrast, a dense structure was observed for NC. (Figure S3a,b). It can be inferred that this unique layered two-dimensional porous carbon structure is due to the decomposition of $\text{Zn}(\text{NO}_3)_2$ at high temperatures. The nitrogen (N_2) adsorption and desorption curves and pore size distribution of 2D-PNC and NC are illustrated in Figure 3c. It can be observed that the isotherm of 2D-PNC shows a clear type-IV hysteresis loop, which is in good agreement with the porous structure shown in SEM (Figure 3a,b). Meanwhile, the unique layered porous structure of 2D-PNC has a higher specific surface area ($534 \text{ m}^2/\text{g}$), which is more conducive to electrolyte impregnation. The TEM images of 2D-PNC (Figure 3d,e) also clearly show the two-dimensional layered porous structure. Figure 3f and its inset show indistinct lattice fringes and blurry diffraction rings of 2D-PNC, showing typical amorphous carbon features, indicating the low degree of graphitization, in good agreement with the results of XRD patterns. Figure 3g illustrates energy-dispersive X-ray spectroscopy (EDS) mapping images demonstrating the uniform distribution of C, N, O, and Zn in two-dimensional layered porous carbon.

To investigate the lithium-ion storage properties of NC and 2D-PNC, we evaluated the electrochemical performances of NC and 2D-PNC as the anode materials of LIBs in a half-cell structure, respectively. Figures 4a and S4 illustrate the cyclic voltammetry (CV) curves in the 0.01–3.0 V voltage range, with a scan rate of 0.1 mV s^{-1} for the first four cycles. In comparison to the initial cycle, the following cycles show significant differences. This result indicates that the CV curves of 2D-PNC and NC electrodes show clear reduction peaks at 0.55 V and 0.70 V in the first cycle, respectively, and these reduction peaks disappear in the subsequent cycles, which may be due to the solid electrolyte interface (SEI) layer formed on the surface of 2D-PNC and NC by electrolyte decomposition [33]. In subsequent cycles, the broad redox peaks at $\sim 0.01/0.3 \text{ V}$ for 2D-PNC and NC may be related to the insertion and desertion of lithium-ion into interlayers and without phase transition. In following cycles, the CV curves overlap well, showing that the stable SEI layer was formed in the initial cycle. The charge and discharge profiles of 2D-PNC and NC for the first four cycles with a current density of 0.2 A g^{-1} and a cutoff potential window of 0.01–3.0 V (Figures 4b and S5), respectively, in which the voltage plateau is well in accordance with the above CV peaks analysis. In the first cycle of the 2D-PNC and NC electrodes, a distinct voltage plateau appears at 0.55 V and 0.70 V, respectively, corresponding to the formation of the SEI layer. There are barely any other obvious voltage plateaus during the following charge and discharge process due to the pseudocapacitive identity of lithium-ion storage in the 2D-PNC and NC electrodes. Meanwhile, from the second cycle the charge and discharge curves start to overlap significantly, showing significant reversibility of lithiation and delithiation in the 2D-PNC and NC electrodes.

The electrochemical reaction kinetics and associated mechanisms of 2D-PNC in LIBs by CV measurements at different scan rates have been investigated (Figures 4c and S6). With increasing scan rates, peak currents of redox reactions increase gradually, while the shape of the CV curves is well maintained. In addition, the potential differences between the reduction (peak 1) and oxidation (peak 2) peaks are enlarged, indicating enhanced polarization. In general, Equations (1) and (2) can be used to describe the connection between peak current (i_p) and scan rate (v).

$$i_p = av^b \quad (1)$$

$$\log i_p = \log a + b \log v \quad (2)$$

where a and b are constants. The slope of the fitted straight line (the value of b) can be used to determine diffusion-controlled and/or pseudocapacitive processes in lithiation/delithiation. $b = 0.5$ or 1.0 suggests an absolutely diffusion-controlled behavior or capacitive behavior, respectively. According to Table S1, peak currents and scan rates were listed, the calculated b values are 0.88 and 0.78 at peak 1 and peak 2, respectively. According to these results, both pseudocapacitance and ionic diffusion control lithium storage reactions in 2D-PNC, and the process of pseudocapacitance plays a primary role in lithium-ion storage, which could also be the reason for their excellent electrochemical performance.

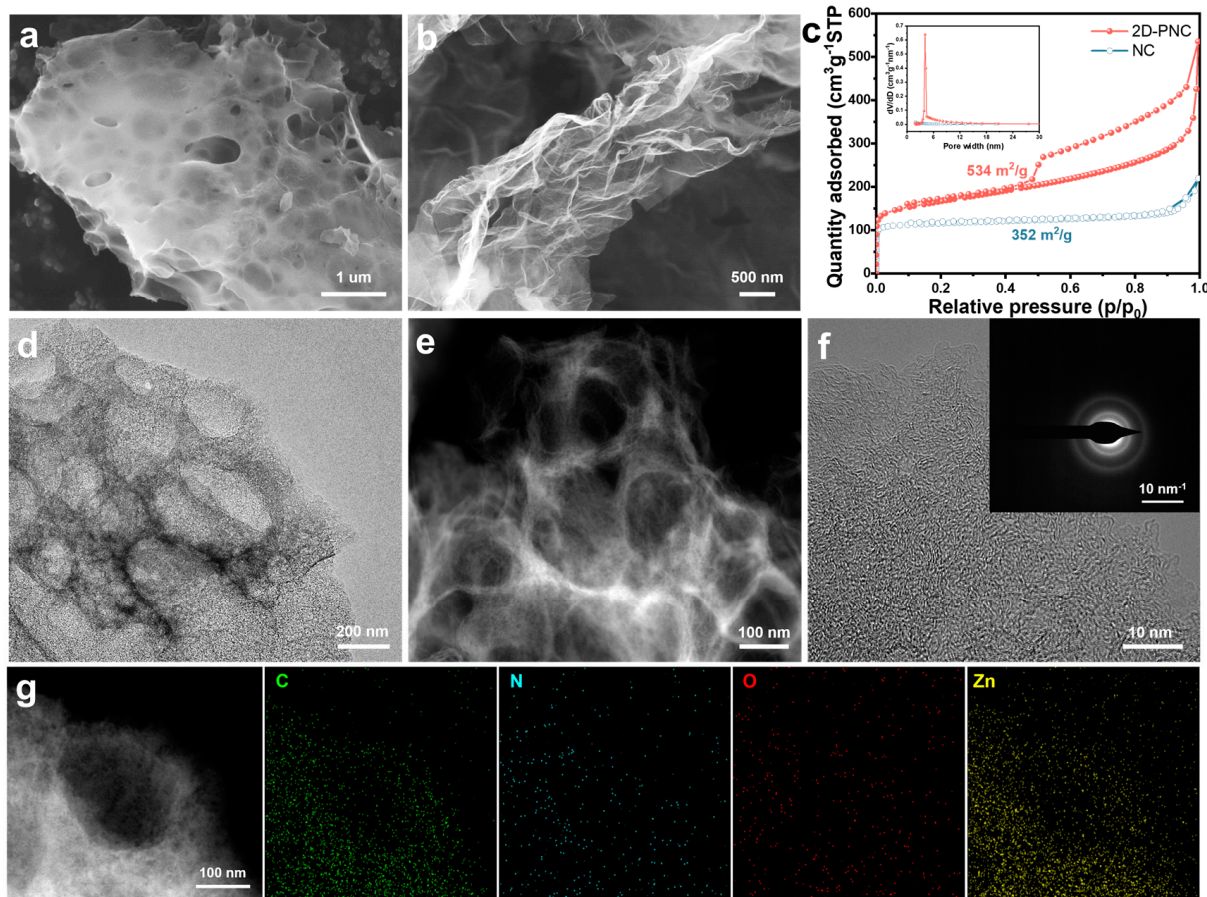


Figure 3. (a,b) SEM images of 2D-PNC. (c) Nitrogen desorption/adsorption isotherms and pore size–distribution curves of 2D-PNC and NC. (d,e) TEM and (f) enlarged TEM images with the SAED pattern. (g) TEM and related energy-dispersive X-ray (EDX) mapping images of 2D-PNC.

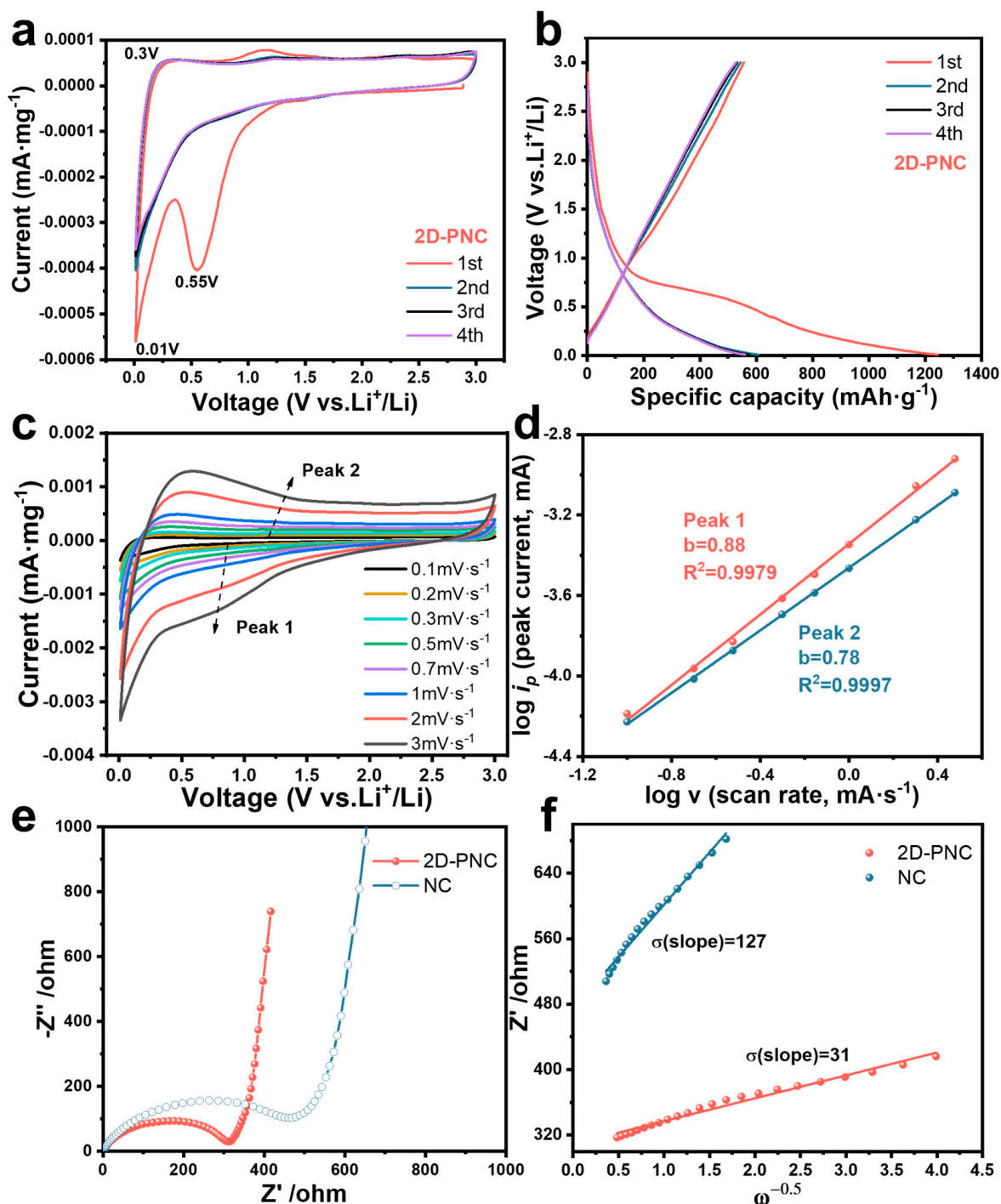


Figure 4. (a) CV profiles of the first four cycles at 0.1 mV s⁻¹ of 2D-PNC. (b) Charge and discharge voltage profiles for the first four cycles at 0.2 A g⁻¹ of 2D-PNC. (c) CV profiles at various scan rates of 2D-PNC, and (d) the corresponding linear fits of 2D-PNC. (e,f) Nyquist plots and the linear fitting plots of Z' vs. $\omega^{-0.5}$ of 2D-PNC.

Subsequently, the electrochemical reaction kinetics were further investigated by electrochemical impedance spectroscopy (EIS). The Nyquist plots of the 2D-PNC and NC electrodes at open circuit potential are illustrated in Figure 4e. It can be observed that both 2D-PNC and NC show a typical semicircle, which correlates with the charge-transfer resistance (R_{ct}) and subsequently corresponds to a straight line of Valborg impedance (W) at low frequency. The R_{ct} of the 2D-PNC electrode (310 Ω) is smaller than those of NC (478 Ω). 2D-PNC electrodes have a higher charge-transfer efficiency than NC electrodes, as

shown by this comparison. Furthermore, the inclined line of the low-frequency region is relevant to the Li^+ diffusion within the electrode. Figure 4f shows linear fitting plots of Z' versus $\omega^{-0.5}$ for the 2D-PNC and NC. It can be observed that the 2D-PNC has a smaller σ , that is, a higher lithium-ion diffusion coefficient (D_{Li^+}), and these results can be ascribed to the unique two-dimensional porous structure of 2D-PNC which enhances the contact area between the electrode and electrolyte, hence ensuring the rapid penetration of the electrolyte, shortening the diffusion path of lithium-ion and accelerating the transfer of lithium-ion.

The rate performances of 2D-PNC and NC in lithium-ion batteries were measured at various current rates ranging from 0.1 to 5.0 A g^{-1} (Figures 5a,b and S7). At the current density of 0.1 A g^{-1} , the reversible capacity of 2D-PNC is 816 mAh g^{-1} . When the current rates are increased to 0.3, 0.5, 1.0, 3.0, and 5.0 A g^{-1} , the specific capacities are 643, 490, 409, 302, and 242 mAh g^{-1} , respectively. The reversible capacity increases to 609 mAh g^{-1} once the current rate goes back to 0.3 A g^{-1} , which is slightly greater than the initial value. This can be explained by the electrode being activated. At current rates of 0.1, 0.3, 0.5, 1.0, 3.0, and 5.0 A g^{-1} , the reversible capacities of NC are 294, 204, 177, 157, 122, and 110 mAh g^{-1} , respectively, which are all inferior to the 2D-PNC exhibited. This is related to the unique 2D porous structure shown by 2D-PNC, which can accelerate the transport of lithium ions and electrons.

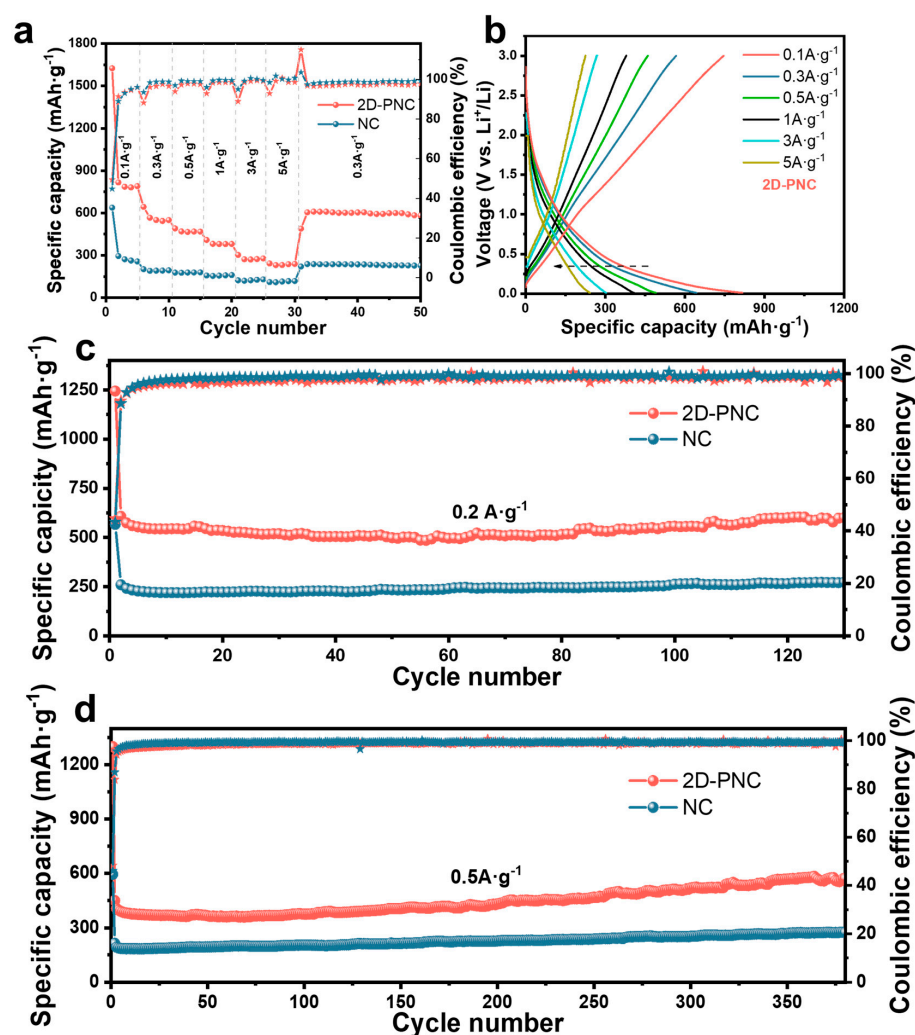


Figure 5. (a) Rate performances of 2D-PNC and NC and (b) the corresponding voltage curves at different current densities from 0.1 to 5 A g^{-1} of 2D-PNC. (c,d) Cycling performances at 0.2 A g^{-1} and 0.5 A g^{-1} of 2D-PNC and NC.

The cycling performance and Coulomb efficiency (CE) of the prepared electrodes were measured at 0.2 A g^{-1} and 0.5 A g^{-1} . As shown in Figure 5c, after 130 consecutive cycles, the reversible specific capacity of 2D-PNC still reaches 600 mAh g^{-1} at a current rate of 0.2 A g^{-1} , which is greater than the 273 mAh g^{-1} of NC. At 0.5 A g^{-1} , the specific capacities of 2D-PNC and NC reach 573 mAh g^{-1} and 274 mAh g^{-1} after 380 cycles, respectively. This can be attributed to the unique two-dimensional layered porous structure of 2D-PNC, which provides more active sites for lithium storage and facilitates the insertion and desorption of lithium ion. The CE of the 2D-PNC electrode reaches almost 100% after several cycles, both at 0.2 A g^{-1} and 0.5 A g^{-1} , which means that it has remarkable structural reversibility.

4. Conclusions

In summary, we used a simple solution stirring strategy to generate COF by a Schiff base reaction in a nonaqueous solvent, and used as-prepared COF as the precursor to produce two-dimensional layered porous carbon materials for LIBs. This carbon material consists of stacked ultrathin carbon nanosheets and has a rich pore structure, high specific surface area, and enriched N atom doping. These features provide better contact between the electrode material and the electrolyte, which shortens the lithium-ion transport distance and can offer more active sites for lithium-ion insertion. The anode of LIBs based on this unique two-dimensional layered porous carbon material can provide not only high cycle reversible capacities (600 mAh g^{-1} after 130 cycles at 0.2 A g^{-1} and 573 mAh g^{-1} after 380 cycles at 0.5 A g^{-1}) but also remarkable rate performance (242 mAh g^{-1} at 5.0 A g^{-1}). This work demonstrates a simple synthesis method for making two-dimensional layered porous carbon materials for LIBs with COF generated by the Schiff base reaction.

Supplementary Materials: The following supporting information can be downloaded at: <https://www.mdpi.com/article/10.3390/en16041733/s1>, Figure S1: FTIR of COF, NC, and 2D-PNC. Figure S2: Zn 2P XPS spectra of the 2D-PNC; Figure S3: (a,b) SEM images of NC; Figure S4: CV curves for the first four cycles at 0.1 mV s^{-1} of NC; Figure S5: Charge and discharge voltage curves for the first four cycles at 0.2 A g^{-1} of NC. Figure S6: The zoomed-in figures of CV curves of 2D-PNC at different scan rates. Figure S7: The corresponding voltage profiles at various current densities from 0.1 to 5 A g^{-1} of NC. Table S1. The values of different scan rates (mV s^{-1}) and the corresponding current peaks ($\text{mA} \cdot \text{mg}^{-1}$).

Author Contributions: Conceptualization, Z.L.; methodology, M.L. and Z.C.; software, M.L., Y.T. and J.H.; investigation, M.L., Y.T., Y.C. and Z.C.; resources, M.L., Z.C. and J.S.; data curation, M.L. and Y.C.; writing—original draft preparation, M.L.; writing—review and editing, Z.L. and Y.B.; supervision, Y.B. and Z.L.; project administration, Z.L.; funding acquisition, Z.L. All authors have read and agreed to the published version of the manuscript.

Funding: This work was supported by the National Natural Science Foundation of China (Grant Nos. 21905152), the Youth Innovation Team Project for Talent Introduction and Cultivation in Universities of Shandong Province, the Taishan Scholar Project of Shandong Province of China, and the China Postdoctoral Science Foundation (Grant Nos. 2022M713249).

Data Availability Statement: All data are available from the corresponding author on reasonable request.

Conflicts of Interest: The authors declare no conflict of interest.

References

1. Lai, X.; Halpert, J.E.; Wang, D. Recent advances in micro-/nano-structured hollow spheres for energy applications: From simple to complex systems. *Energy Environ. Sci.* **2012**, *5*, 5604–5618. [[CrossRef](#)]
2. Lee, S.-M.; Kim, J.; Moon, J.; Jung, K.-N.; Kim, J.H.; Park, G.-J.; Choi, J.-H.; Rhee, D.Y.; Kim, J.-S.; Lee, J.-W.; et al. A cooperative biphasic MoOx-MoPx promoter enables a fast-charging lithium-ion battery. *Nat. Commun.* **2021**, *12*, 39. [[CrossRef](#)] [[PubMed](#)]
3. Fan, L.; Lei, S.; Kheimeh Sari, H.M.; Zhong, L.; Kakimov, A.; Wang, J.; Chen, J.; Liu, D.; Huang, L.; Hu, J.; et al. Controllable S-Vacancies of monolayered Mo-S nanocrystals for highly harvesting lithium storage. *Nano Energy* **2020**, *78*, 105235. [[CrossRef](#)]
4. Bruce, P.G.; Scrosati, B.; Tarascon, J.-M. Nanomaterials for Rechargeable Lithium Batteries. *Angew. Chem. Int. Ed.* **2008**, *47*, 2930–2946. [[CrossRef](#)]

5. Chen, L.-F.; Ma, S.-X.; Lu, S.; Feng, Y.; Zhang, J.; Xin, S.; Yu, S.-H. Biotemplate synthesis of three-dimensional porous MnO/C-N nanocomposites from renewable rapeseed flower pollen: An anode material for lithium-ion batteries. *Nano Res.* **2016**, *10*, 1–10. [[CrossRef](#)]
6. Tarascon, J.M.; Armand, M. Issues and challenges facing rechargeable lithium batteries. *Nature* **2001**, *414*, 359–367. [[CrossRef](#)]
7. Ghigna, P.; Airoldi, L.; Fracchia, M.; Callegari, D.; Anselmi-Tamburini, U.; D'Angelo, P.; Pianta, N.; Ruffo, R.; Cibin, G.; de Souza, D.O.; et al. Lithiation Mechanism in High-Entropy Oxides as Anode Materials for Li-Ion Batteries: An Operando XAS Study. *ACS Appl. Mater. Interfaces* **2020**, *12*, 50344–50354. [[CrossRef](#)]
8. Yu, K.; Wang, Y.; Wang, X.; Liu, W.; Liang, J.; Liang, C. Preparation of porous carbon anode materials for lithium-ion battery from rice husk. *Mater. Lett.* **2019**, *253*, 405–408. [[CrossRef](#)]
9. Xu, K.; Li, Y.; Xiong, J.; Ou, X.; Su, W.; Zhong, G.; Yang, C. Activated Amorphous Carbon With High-Porosity Derived From Camellia Pollen Grains as Anode Materials for Lithium/Sodium Ion Batteries. *Front. Chem.* **2018**, *6*, 366. [[CrossRef](#)]
10. Xu, C.; Wei, Q.; Li, M.; You, J.; Song, W.; Wang, X.; Zhang, G.; Li, H.; He, Y.; Liu, Z. Ultrafast and simple integration engineering of graphene-based flexible films with extensive tunability and simple trial in lithium-ion batteries. *J. Alloys Compd.* **2022**, *922*, 166282. [[CrossRef](#)]
11. Sun, D.; Yang, J.; Yan, X. Hierarchically porous and nitrogen, sulfur-codoped graphene-like microspheres as a high capacity anode for lithium ion batteries. *Chem. Commun.* **2015**, *51*, 2134–2137. [[CrossRef](#)]
12. Fu, L.; Tang, K.; Song, K.; van Aken, P.A.; Yu, Y.; Maier, J. Nitrogen doped porous carbon fibres as anode materials for sodium ion batteries with excellent rate performance. *Nanoscale* **2014**, *6*, 1384–1389. [[CrossRef](#)]
13. Zheng, F.; Liu, D.; Xia, G.; Yang, Y.; Liu, T.; Wu, M.; Chen, Q. Biomass waste inspired nitrogen-doped porous carbon materials as high-performance anode for lithium-ion batteries. *J. Alloys Compd.* **2017**, *693*, 1197–1204. [[CrossRef](#)]
14. Alkarmo, W.; Ouhib, F.; Aqil, A.; Thomassin, J.-M.; Vertruyen, B.; Piedboeuf, M.-L.; Job, N.; Detrembleur, C.; Jérôme, C. Continuous-porous N-doped carbon network as high-performance electrode for lithium-ion batteries. *J. Mater. Sci.* **2018**, *53*, 6135–6146. [[CrossRef](#)]
15. Gomez-Martin, A.; Martinez-Fernandez, J.; Rutttert, M.; Winter, M.; Placke, T.; Ramirez-Rico, J. An electrochemical evaluation of nitrogen-doped carbons as anodes for lithium ion batteries. *Carbon* **2020**, *164*, 261–271. [[CrossRef](#)]
16. Bhattacharjya, D.; Park, H.-Y.; Kim, M.-S.; Choi, H.-S.; Inamdar, S.N.; Yu, J.-S. Nitrogen-Doped Carbon Nanoparticles by Flame Synthesis as Anode Material for Rechargeable Lithium-Ion Batteries. *Langmuir* **2014**, *30*, 318–324. [[CrossRef](#)]
17. Wang, Z.-L.; Xu, D.; Wang, H.-G.; Wu, Z.; Zhang, X.-B. In Situ Fabrication of Porous Graphene Electrodes for High-Performance Energy Storage. *ACS Nano* **2013**, *7*, 2422–2430. [[CrossRef](#)]
18. Wang, P.; Wu, Q.; Han, L.; Wang, S.; Fang, S.; Zhang, Z.; Sun, S. Synthesis of conjugated covalent organic frameworks/graphene composite for supercapacitor electrodes. *RSC Adv.* **2015**, *5*, 27290–27294. [[CrossRef](#)]
19. Fang, Q.; Gu, S.; Zheng, J.; Zhuang, Z.; Qiu, S.; Yan, Y. 3D Microporous Base-Functionalized Covalent Organic Frameworks for Size-Selective Catalysis. *Angew. Chem. Int. Ed.* **2014**, *53*, 2878–2882. [[CrossRef](#)]
20. Côté, A.P.; Benin, A.I.; Ockwig, N.W.; O'Keeffe, M.; Matzger, A.J.; Yaghi, O.M. Porous, Crystalline, Covalent Organic Frameworks. *Science* **2005**, *310*, 1166–1170. [[CrossRef](#)]
21. Ibrahim, M.; Fayed, M.G.; Mohamed, S.G.; Wen, Z.; Sun, X.; Abdelhamid, H.N. High-Performance Lithium-Ion Battery and Supercapacitors Using Covalent Organic Frameworks (COFs)/Graphitic Carbon Nitride (g-C₃N₄)-Derived Hierarchical N-Doped Carbon. *ACS Appl. Energy Mater.* **2022**, *5*, 12828–12836. [[CrossRef](#)]
22. Zhuang, G.-L.; Gao, Y.-F.; Zhou, X.; Tao, X.-Y.; Luo, J.-M.; Gao, Y.-J.; Yan, Y.-L.; Gao, P.-Y.; Zhong, X.; Wang, J.-G. ZIF-67/COF-derived highly dispersed Co₃O₄/N-doped porous carbon with excellent performance for oxygen evolution reaction and Li-ion batteries. *Chem. Eng. J.* **2017**, *330*, 1255–1264. [[CrossRef](#)]
23. Li, Z.; Ji, W.; Wang, T.-X.; Zhang, Y.; Li, Z.; Ding, X.; Han, B.-H.; Feng, W. Guiding Uniformly Distributed Li-Ion Flux by Lithiophilic Covalent Organic Framework Interlayers for High-Performance Lithium Metal Anodes. *ACS Appl. Mater. Interfaces* **2021**, *13*, 22586–22596. [[CrossRef](#)] [[PubMed](#)]
24. Caballero, A.; Hernán, L.; Morales, J. Limitations of Disordered Carbons Obtained from Biomass as Anodes for Real Lithium-Ion Batteries. *ChemSusChem* **2011**, *4*, 658–663. [[CrossRef](#)]
25. Boonprachai, R.; Autthawong, T.; Namsar, O.; Yodbunork, C.; Yodying, W.; Sarakonsri, T. Natural Porous Carbon Derived from Popped Rice as Anode Materials for Lithium-Ion Batteries. *Crystals* **2022**, *12*, 223. [[CrossRef](#)]
26. Gou, W.; Kong, X.; Wang, Y.; Ai, Y.; Liang, S.; Pan, A.; Cao, G. Yolk-shell structured V₂O₃ microspheres wrapped in N, S co-doped carbon as pea-pod nanofibers for high-capacity lithium ion batteries. *Chem. Eng. J.* **2019**, *374*, 545–553. [[CrossRef](#)]
27. Yang, Z.; Duan, X.; Wang, J.; Li, Y.; Fan, X.; Zhang, F.; Zhang, G.; Peng, W. Facile Synthesis of High-Performance Nitrogen-Doped Hierarchically Porous Carbon for Catalytic Oxidation. *ACS Sustain. Chem. Eng.* **2020**, *8*, 4236–4243. [[CrossRef](#)]
28. Li, J.; Chen, S.; Yang, N.; Deng, M.; Ibraheem, S.; Deng, J.; Li, J.; Li, L.; Wei, Z. Ultrahigh-Loading Zinc Single-Atom Catalyst for Highly Efficient Oxygen Reduction in Both Acidic and Alkaline Media. *Angew. Chem. Int. Ed.* **2019**, *58*, 7035–7039. [[CrossRef](#)]
29. Li, Z.; Wang, D.; Li, H.; Ma, M.; Zhang, Y.; Yan, Z.; Agnoli, S.; Zhang, G.; Sun, X. Single-atom Zn for boosting supercapacitor performance. *Nano Res.* **2022**, *15*, 1715–1724. [[CrossRef](#)]
30. Fang, Y.; Zeng, Y.; Jin, Q.; Lu, X.F.; Luan, D.; Zhang, X.; Lou, X.W. Nitrogen-Doped Amorphous Zn–Carbon Multichannel Fibers for Stable Lithium Metal Anodes. *Angew. Chem. Int. Ed.* **2021**, *60*, 8515–8520. [[CrossRef](#)]

31. Zheng, W.; Chen, F.; Zeng, Q.; Li, Z.; Yang, B.; Lei, L.; Zhang, Q.; He, F.; Wu, X.; Hou, Y. A Universal Principle to Accurately Synthesize Atomically Dispersed Metal–N₄ Sites for CO₂ Electroreduction. *Nanomicro Lett.* **2020**, *12*, 108.
32. Bian, Z.; Yuan, T.; Xu, Y.; Pang, Y.; Yao, H.; Li, J.; Yang, J.; Zheng, S. Boosting Li–S battery by rational design of freestanding cathode with enriched anchoring and catalytic N-sites carbonaceous host. *Carbon* **2019**, *150*, 216–223. [[CrossRef](#)]
33. Yang, L.X.; Liu, R.J.; Bu, H.P.; Liu, H.J.; Zeng, C.L.; Fu, C. TiC Nanomaterials with Varying Dimensionalities as Anode Materials for Lithium-Ion Batteries. *ACS Appl. Nano Mater.* **2022**, *5*, 11787–11796. [[CrossRef](#)]

Disclaimer/Publisher’s Note: The statements, opinions and data contained in all publications are solely those of the individual author(s) and contributor(s) and not of MDPI and/or the editor(s). MDPI and/or the editor(s) disclaim responsibility for any injury to people or property resulting from any ideas, methods, instructions or products referred to in the content.